

Asian Summer Monsoon Anticyclone: Trends and Variability

Ghouse Basha¹, M. Venkat Ratnam¹ and Pangaluru Kishore²

¹National Atmospheric Research Laboratory, Department of Space, Gadanki-517112, India.

² Department of Earth System Science, University of California, Irvine, CA, 92697, USA.

Correspondence to: Ghouse Basha (mdbasha@narl.gov.in)

Abstract

The Asian Summer Monsoon Anticyclone (ASMA) has been a topic of intensive research in recent times through its variability in dynamics, chemistry and radiation. This work explores the spatial variability and the trends of the ASMA using observational and reanalysis data sets. Our analysis indicates that the spatial extent and magnitude of ASMA is greater during July and August compared to June and September. The decadal variability of the anticyclone is very large at the edges of the anticyclone than at the core region. Significant decadal variability is observed in the northeast and southwest parts of ASMA with reference to the 1951-1960 period. The strength of the ASMA shows a drastic increase in zonal wind anomalies in terms of temporal variation. Further, our results show that the extent of the anticyclone is greater during the active phase of the monsoon, strong monsoon years, and La Niña events. Significant warming with strong westerlies is observed exactly over the Tibetan Plateau from the surface to tropopause during the active phase of the monsoon, strong monsoon years, and during La Niña events. Our results support the transport process over Tibetan Plateau and the Indian region during active, strong monsoon years and during strong La Niña years. It is suggested to consider different phases of monsoon while interpreting the variability of pollutants/trace gases in the anticyclone.

Keywords: Asian Monsoon, anticyclone, geopotential height, La Niña, El Niño, and rainfall.

27 **1. Introduction**

28 The Asian Summer Monsoon Anticyclone (ASMA) is a dominant circulation in the
29 Northern Hemisphere (NH) summer in the Upper Troposphere and Lower Stratosphere
30 (UTLS), which extends from Asia to the Middle East. ASMA is bordered by the subtropical
31 westerly jet in the north and easterly jets to the south. The Asian Summer Monsoon (ASM)
32 dynamics act as a pathway for the transport of trace gases and pollutants both vertically
33 (through convection) and horizontally (through low-level jet and tropical easterly jet). The
34 ASMA circulation responds to heating corresponding to the deep convection of the south
35 Asian monsoon (Hoskins and Rodwell, 1995; Highwood and Hoskins, 1998). This strong
36 anticyclone circulation isolates the air and is tied to the outflow of deep convection, which
37 has distinct maximum characteristics in terms of dynamical and chemical variability (Randel
38 and Park, 2006; Park et al., 2007). Recently, the anticyclone circulation in UTLS has been
39 paid more attention by researchers in order to understand the dynamics, chemistry, and
40 radiation of the region. This problem has been discussed by several authors (e.g., Park et al.,
41 2007; Fadnavis et al., 2014; Glatthor et al., 2015; Vernier et al., 2015; Santee et al., 2017).
42 Deep convection during monsoon can transport tropospheric tracers from the surface to the
43 UTLS (Vogel et al., 2015; Tissier and Legras, 2016). The tracers which are transported are
44 confined in the anticyclone will affect the trace gas concentration in the UTLS resulting in
45 significant changes in radiative forcings (Solomon et al., 2010; Riese et al., 2012; Hossaini et
46 al., 2015). The center of the anticyclone is located either over the Iranian Plateau or over the
47 Tibetan Plateau where the distribution of pollutants and tracers vary significantly (Yan et al.,
48 2011).

49 The spatial extent, strength, and the location of an anticyclone vary on several
50 temporal scales caused by internal dynamical variability of the Asian monsoon (Zhang et al.,
51 2002; Randel and Park, 2006; Garny and Randel, 2013; Vogel et al., 2015; Pan et al., 2016).

52 However, the variability of the anticyclone structure and response to Indian monsoon activity
53 are not understood. Further, the tracers (O₃, and CO etc.) trapped in the anticyclone during
54 the same period in the UTLS region. Since the anticyclone extends from the Middle East to
55 East Asia, trapped pollutants are expected to make a large radiative forcing to the background
56 atmosphere. Thus, it is essential to understand the variability of anticyclone structure itself in
57 detail and its response to Indian Summer Monsoon (ISM). Therefore, in the first part of the
58 study, we investigate the spatial, inter-annual and decadal variations of the anticyclone. Since
59 the Indian monsoon responds at different time scales, we also investigated the anticyclone
60 variability with respect to the active and break spells of the Indian monsoon, strong and weak
61 monsoon years, and the stronger El Nino Southern Oscillation (ENSO) years. For this, we
62 have utilized the NCEP/NCAR reanalysis geopotential height from 1951 to 2016. The
63 structure of the paper is as follows. We describe the data sets used in this study in Section 2.
64 Section 3 contains the seasonal and decadal variation of the anticyclone. Section 4 shows the
65 influence of ISM on anticyclone i.e. active and break spells, strong and weak monsoon years,
66 and ENSO's effects on the anticyclone. Finally, we discuss our results presented in Section 5.

67 **2. Data and Methodology**

68 **2.1. NCEP/NCAR Reanalysis**

69 The National Center for Environmental Prediction (NCEP), in collaboration with the
70 National Center for Atmospheric Research (NCAR) produces reanalysis data from a
71 consistent assimilation and modeling procedure that incorporates all the available observed
72 conditions obtained from conventional and satellite information from 1951 to the present
73 (Kalnay et al. 1996). We used NCEP/NCAR reanalysis daily geopotential height (GPH) and
74 wind data from the years 1951 to 2016. The NCEP/NCAR data assimilation uses a 3D-
75 variational analysis scheme with 28 pressure levels and triangular truncation of 62 waves
76 (horizontal resolution of 200m). Both GPH and temperature at the chosen standard levels are

77 described as class output variables (Kalnay et al. 1996) i.e. they are strongly influenced by
78 observed data. Only the Indian summer monsoon months (June, July, and August,
79 September) containing gridded daily data were considered in this study. The NCEP/NCAR
80 reanalysis data had a spatial resolution of 2.5° . The seasonal values are estimated from daily
81 data. To identify the spatial and temporal variations of the anticyclone center, we used the
82 monthly mean values of the GPH and the zonal wind component. The quality of NCEP GPH
83 reanalysis data can be found from Bromwich et al. (2007).

84 **2.2. IMD Gridded Precipitation Data**

85 The India Meteorological Department (IMD) high-resolution ($0.25^\circ \times 0.25^\circ$) gridded
86 precipitation data is used to identify the active and break spells during June, July and August
87 months from 1951-2016 (Pai et al. 2016). This precipitation data has been validated
88 extensively with observational and reanalysis data sets and displays a very good correlation
89 (Kishore et al., 2016). Data from 1951-2016 have been used. We have identified the active
90 and break spells based on daily rainfall over monsoon core zone of India (which is roughly
91 from 18°N to 28°N and 65°E to 88°E) during July and August months as reported by
92 Rajeevan et al. (2010). The normalized anomaly is estimated from the averaged daily rainfall
93 in the monsoon core zone is subtracted from its long term (1951-2000) mean and by dividing
94 with its daily standard deviation. The active (break) spells were identified from the
95 normalized anomaly when rainfall is greater (lesser) than -1.0 ($+1.0$), consecutively for three
96 days or more. Data from 1951-2016 have been used.

97 **2.3. GNSS Radio Occultation (RO) Data**

98 We have also used the Global Navigation Satellite System (GNSS) Radio Occultation
99 (RO) data for investigating the temperature anomaly. The basic measurement principle of RO
100 exploits the atmosphere-induced phase delay in the GNSS signals, which are recorded in the
101 low earth-orbiting satellite. This technique provides vertical profiles of refractivity, density,

102 pressure, temperature, and water vapor (Kursinski et al., 1997). The temperature profiles
103 from this technique are available with low horizontal (~200-300 km) and high vertical
104 resolutions (10-35 km) with an accuracy of <0.5 K. We used the CHALLENGING Minisatellite
105 Payload (CHAMP) and Constellation Observing System for Meteorology, Ionosphere, and
106 Climate (COSMIC) covering the period from 2002 to 2016.

107 The CHAMP satellite was launched on 15 July 2000 into a circular orbit by Germany
108 to measure the Earth's gravity and magnetic field and to provide global RO soundings
109 (Wickert et al. 2001). About ~230 RO profiles per day were measured by the CHAMP
110 payload since 2002. The CHAMP payload was solely designed to track the setting
111 occultations, and the RO event gets terminated when the signal is lost, which results in a
112 decrease in the number of occultations with a decreasing altitude (Beyerle et al. 2006). This
113 receiver measures the phase delay of radio wave signals that are occulted by the Earth's
114 atmosphere. From this phase delay, it is possible to retrieve the bending angle and refractivity
115 vertical profiles.

116 COSMIC consists of a constellation of 6 satellites, which was launched in April 2006
117 to a circular, 72° inclination orbit at a 512 km altitude capable of receiving signals from the
118 Global Positioning System (GPS) (Anthes et al., 2008). Compared to previous satellites,
119 COSMIC satellites employed an open loop mode, which can track both the rising and setting
120 of occultations (Schreiner et al. 2007). The open-loop tracking technique significantly
121 reduces the GPS RO inversion biases by eliminating tracking errors (Sokolovskiy et al.
122 2006). The COSMIC temperature profiles display a very good agreement with radiosonde
123 data, reanalyses, and models (Rao et al., 2009; Kishore et al., 2011; Kishore et al., 2016). The
124 CHAMP and COSMIC GPSRO data was interpolated to 200 m from their native resolution.
125 We derived the cold point tropopause altitude/temperature over the ASMA region as
126 discussed by Ratnam et al. (2014) and Ravindrababu et al. (2015). Both the CHAMP and

127 COSMIC data were obtained from COSMIC Data Analysis and Archive Center (CDAAC)
128 (<https://cdaac-www.cosmic.ucar.edu/cdaac/products.html>).

129 **3. Results and Discussion**

130 **3.1. Variability of the Anticyclone**

131 The climatological spatial variability of the GPH and wind vectors at 100 hPa during
132 June, July, August and September months from NCEP reanalysis data is shown in Figure 1(a,
133 b, c & d). The anticyclone circulation is clearly depicted during June, July, August, and
134 September by wind vectors (Figure 1). During the month of September and June, the values
135 of GPH are low compared to July and August which represents the spatial extent of the
136 anticyclone. The spatial extent and intensity of the anticyclone are greater during July
137 compared to the other months. During July and August, the anticyclone extends from East
138 Asia to the Middle East. The spatial extent of the anticyclone circulation is clearly evident in
139 the grid 15°N-45°N; 30°E-120°E at 100 hPa level and the climatological averaged values of
140 GPH varies from 16.5-17 km in NCEP reanalysis during 1951-2016. Using the modified
141 potential vorticity equation, Randel et al. (2006) showed the spatial variation of the
142 anticyclone where GPH values are stationary in the range of 16.75-16.9 km. Similarly, Park
143 et al. (2007) showed the anticyclone structure from the strongest wind at 100 hPa through
144 streamline function. Bian et al. (2012) reported the spatial variability of the anticyclone using
145 16.77 km and 16.90 km in the GPH contour as the lower and the upper boundary,
146 respectively. Thus, these empirically selected GPH values represent the anticyclone
147 boundaries. Therefore, in this present study, we have chosen the values from 16.75 to 16.9
148 km to investigate the spatial features of the anticyclone and the resultant picture is depicted in
149 Figure 1(e, f, g & h). The spatial extent and existence of the anticyclone are highly prominent
150 during July and August compared to June. During the September month, very low values of
151 GPH are seen compared to July and August. Therefore, we considered the average of July

152 and August GPH from 1951-2016 for further analysis as shown in Figure S1. The core region
153 and the spatial extent of the anticyclone are clearly evident from Figure S1. The core region
154 of the anticyclone shows bimodal distribution i.e. one core located at the south-western flank
155 of the Himalayas and another over Iran. The core region over the south-western flank of
156 Himalayas is due to large scale updraft, which is caused by the moist energy over Indo-
157 Gangetic plain, heating of Tibetan plateau, and the orographic forcing of the Himalayas.
158 Severe heating over Arabian Peninsula supports the formation of the mid-tropospheric the
159 anticyclone in the west. This anticyclone can merge intermittently within ASMA. It is also
160 observed that the spatial extent of the anticyclone varies drastically at different temporal
161 scales. Therefore, seasonal variation is much more pronounced.

162 The decadal variation of the anticyclone is studied with respect to the spatial
163 variability. Figure 2 shows the decadal spatial variation of the anticyclone with reference to
164 the years 1951-1960. The significant difference in the decadal variation is noticed in Figure 2.
165 The edges (east, north, and west) of the anticyclone undergo drastic changes during the
166 period 1961-1970. In case of 1971-1980 period, except for a small portion in the east, the
167 whole anticyclone shows drastic changes. During the decade 1971-1980, the recorded GPH
168 values in the anticyclone are lower by ~ 25 m when compared to the values in 1951-1960.
169 This feature is quite opposite during 1981-1990 where high values (~ 30 m) are observed
170 compared to those in the reference period. The GPH difference is significant over the west,
171 northeast and southern regions of the anticyclone during the 1991-2000 period. Similar
172 changes are observed during 2001-2010. Compared to all the decadal differences, 2011-2016
173 shows a completely different picture. The changes are only in the western and north-eastern
174 corner, whereas other parts of the anticyclone do not show any change. From this analysis,
175 we observed significant changes in the anticyclone even from one decade to another, which
176 can result in a change in chemical and dynamical changes over this region.

177 Further, the spatial distribution of trend is estimated during the years 1951-2016 by
178 using robust regression analysis at 95% confidence interval as displayed in Figure 3. The
179 edges on all sides of the anticyclone undergo noticeable changes compared to the core region.
180 The east and north-west side of the anticyclone shows an increasing trend compared to other
181 regions. The trends at the northern end are significant than the southern end. A few portions
182 on the northern side of the anticyclone show a reduction in the strength. Therefore, in order to
183 understand the asymmetry in the anticyclone variability, we have divided the anticyclone
184 region into 4 different sectors as shown in Figure 4 based on the peak values of GPH along
185 longitude and latitude cross-sections. The center values of GPH are located at 70°E longitude
186 and 32.5°N Latitude. The four sectors can be divided into South-East (SE) (22.5°N-32.5°N),
187 North-East (NE) (32.5°N-40°N) in the longitude band of 70°E-120°E, South-West (SW)
188 (22.5°N-32.5°N), and North-West (NW) (32.5°N-40°N) at the 20°E-70°E longitude range.
189 The area-averaged time series (July and August) of zonal wind anomalies in these sectors
190 from 1951-2016 are shown in Figure 5. The zonal wind anomalies show a clearly increasing
191 trend in all the sectors. From the year 1951 to 1980, the zonal wind anomalies are negative
192 and shift to positive in all the sectors. The year 1980 represents the beginning of
193 industrialization globally (Basha et al., 2017). The change is highly significant in the north-
194 west and north-east sectors with a magnitude variability of 7.59 m/s from 1951-2016 whereas
195 it is 5.44 m/s in the south-east and south-west sectors. In addition, we estimated the strength
196 of the anticyclone during the monsoon season by using a difference in the zonal wind
197 between the northern (30°N-40°N) and southern (10°N-20°N) flanks of the anticyclone,
198 which is depicted in Figure 5e. A significant increase in the strength of the anticyclone is
199 noticed from Figure 5e at a rate of 0.157 m/s per year (10.36 m/s from 1951-2016).

200 It is well known that the Indian monsoon rainfall varies at different time scales i.e.
201 daily, sub-seasonal, interannual, decadal and centennial scales (Rajeevan et al., 2010).

202 Precipitation during the monsoon varies from intra-seasonal scales between active (good
203 rainfall) and break (less rainfall) spells. Any small change in the precipitation pattern will
204 affect the anticyclone due to the thermodynamics involved in rainfall. In this study, we also
205 investigated the anticyclone variability during the active and break spells of the Indian
206 monsoon. The active and break spells were identified in July and August by using the high
207 resolution gridded ($0.25^\circ \times 0.25^\circ$) rainfall data from 1951 to 2016 as defined by Pai et al.
208 (2016).

209 The number of active and break days is derived from the precipitation data shown in
210 Figure S2 (a & b). Daily GPH, temperature, and zonal wind are taken from NCEP reanalysis
211 whereas the tropopause altitude is derived from the GNSS RO data for active and break days.
212 The anticyclone structure during active (red line) and break (blue line) days are shown in
213 Figure 6a. Two interesting aspects of the anticyclone variability can be noticed between
214 active and break days. One aspect is the extent of the anticyclone is large during active days
215 compared to break days and another is the existence of two cell structures in the anticyclone
216 core region during active days. The extent is large in the eastern and northern side in active
217 days. The zonal (meridional) cross-section of temperature (color shade), zonal wind (contour
218 lines) difference between active and break phase averaged in the longitude band of 80°E - 90°E
219 (latitude band of 30°N - 40°N) along with cold point tropopause for active and break days is
220 illustrated in Figures 6b & 6c. During active days, temperature shows cooling in tropical
221 latitudes whereas it shows warming in the mid-latitudes from surface to the tropopause.
222 Significant warming is observed during the active days in the mid-troposphere over the
223 Tibetan Plateau and its northern side. Westerly (easterly) winds exist over the cooler
224 (warmer) regions. The warm temperature anomalies stretch from 1.5 to 12 km in between
225 25°N and 60°N . The tropopause altitude is low (high) during the active (break) phase of
226 Indian monsoon as shown in Figure 6b. The meridional cross-section of temperature

227 anomalies displays significant warming from ~ 1.5 to 8 km over the Indian region. The
228 tropopause altitude exemplifies random variability in the meridional cross-section.

229 As discussed previously, the anticyclone circulation is significant during the months
230 of July and August when most of the precipitation occurs over India (Basha et al., 2013;
231 Basha et al., 2015; Kishore et al., 2015; Narendra Reddy et al., 2018). The influence of strong
232 and weak monsoon years will have a drastic impact on anticyclone circulation. In order to
233 understand these changes, we have divided the years into strong and weak monsoon years
234 based on gridded precipitation data over the domain 5°N - 30°N and 70°E - 95°E from the years
235 1951-2016. This region is known to have heavy precipitation and orographic forcing, which
236 helps transport of water vapor through deep convection to UTLS (Houze et al., 2007; Medina
237 et al., 2010; Pan et al., 2016). The detrended precipitation represents the strong and weak
238 monsoon years. Years with positive (negative) values of precipitation shows the strong
239 (weak) monsoon years as shown in Figure S2b. The composite of mean distribution of the
240 anticyclone circulation during strong and weak monsoon years is shown in Figure 7a based
241 on GPH values at 100 hPa from NCEP reanalysis data. The circulation expands on the eastern
242 and western sides of the anticyclone during the strong monsoon years (red line). The core of
243 the anticyclone is significant during strong monsoon years. Clear eye structure is observed in
244 the core of the anticyclone on left (right) during the strong (weak) monsoon years. The
245 composite mean difference of temperature and zonal wind between the strong and weak
246 monsoon years along with tropopause altitude averaged in the longitude range of 80 - 85°E is
247 shown in Figure 7b. The warmest temperature anomalies are observed over the Tibetan
248 Plateau. Positive (warm) temperature anomalies exactly above the Tibetan Plateau (11 km)
249 and negative (cooling) on both sides are noticed in the lower troposphere from Figure 7b.
250 Strong easterlies (westerlies) winds are observed on the left (right) side of the Tibetan
251 Plateau. The whole Tibetan Plateau acts as a barrier that drives the cold air to upper altitudes

252 during strong monsoon years. Strong anticyclone circulation with strong westerlies at 35°N
253 and easterlies on both sides with elevated tropopause represent the impacts of the strong
254 monsoon vertically above the anticyclone. The rising motion over East Asia is excited by the
255 local heating of the Tibetan Plateau links to the single stretch vertically. The longitude and
256 altitude cross-section of temperature and wind anomalies shown in Figure 7c are averaged
257 between a latitude band of 35-40°N. Positive temperature anomalies are observed from the
258 surface to 12 km in the longitudes 60-80°E and stretch towards the west. This process clearly
259 demonstrates that a large scale ascent develops over the Asian monsoon region. The
260 tropopause altitude is high (low) during strong vertical motion and heavy precipitation is
261 noticed over the region similar to that reported by Lau et al. (2018). The transport processes
262 from the boundary layer to the tropopause occur on the east side of the anticyclone i.e.
263 southern flank of Tibetan Plateau, northeast India and the head of the Bay of Bengal. This
264 result is consistent with the previous studies by Bergman et al. (2013).

265 ENSO typically shows the strongest signal in boreal winter, but it can affect the
266 atmospheric circulation and constituent distributions until the next autumn (McPhaden et al.,
267 2006). It is well-known that strong ENSO events have a significant influence on tropical
268 upwelling and STE (Yan et al., 2018). This change can impact the distribution of the
269 composition and structure of the UTLS region. In the UTLS region, the tropopause responds
270 to the annual and interannual variability associated with ENSO (Trenberth, 1990) and QBO
271 (Baldwin et al., 2001). Several studies have been focused on the effects of the different
272 impacts of El Niño on tropopause and lower stratosphere (Hu and Pan, 2009; Zubiaurre and
273 Calvo, 2012; Xie et al., 2012). In the present study, we have investigated the changes
274 associated with strong ENSO events with the anticyclone circulation and tropical upwelling
275 during July and August. Therefore, we have also separated the GPH for the strongest El Niño
276 (1958, 1966, 1973, 1983, 1988, 1992, 1998, and 2015) and La Niña (1974, 1976, 1989, 1999,

277 2000, 2008, and 2011) years to verify the change in the circulation pattern of the anticyclone.
278 For this, we have chosen July and August GPH data at 100hPa as shown in Figure 8. The red
279 and blue colors indicate the composite of the La Niña and El Niño circulation. During the La
280 Niña, the anticyclone circulation extends large compared to El Niño years at 100 hPa as
281 shown in the Figure 8a. On the eastern and southern sides of the anticyclone, the expansion is
282 more during the La Niña years. The warm temperature with strong westerlies in the latitude
283 band of 43°N-55°N is observed during La Niña as shown in Figure 8b (Lau et al., 2018). The
284 cooling impact is significant over the Tibetan Plateau during La Niña events compared to El
285 Niño events. Significant cooling is observed over the Tibetan Plateau and distributes towards
286 tropical latitudes between 600-100 hPa. The zonal wind shows a convergence of easterly
287 winds over the Tibetan Plateau from the mid to the upper tropospheric region. On the right
288 side of the Tibetan Plateau there exist strong westerly winds from the surface to the
289 tropopause altitudes with strong warming. The meridional cross-section of temperature and
290 the zonal wind difference between La Niña and El Niño is shown in Figure 8c. Significant
291 cooling is observed during La Niña in the longitude band of 80°E-100°E with strong
292 easterlies from the surface to the tropopause. From this analysis, it is clear that the Indian
293 summer monsoon variability has a significant impact on ASMA, and it is necessary to
294 consider the different phases of monsoon while dealing with UTLS pollutants. In addition,
295 we have investigated the zonal mean vertical cross-section in the longitude band of 50-60°E,
296 which represents the Iranian Mode. Figure S3 depicts the difference between active and break
297 phases, strong and weak monsoon years, and La Niña and El Niño years along with the
298 tropopause altitude. Significant warming is observed during La Niña years and strong
299 monsoon years compared to the active phase of the Indian monsoon in the troposphere.
300 Compared to the Tibetan mode, Iranian mode warming is less. The tropopause altitude is
301 slightly higher during the active phase of the Indian monsoon, strong monsoon years and La

302 Niña years. A moderate increase in tropopause from the equator to 40°N is observed and
303 decreases drastically afterward.

304 **4. Summary and Conclusions**

305 Several authors discussed the interannual and decadal variability of pollutants and tracers
306 in the ASMA region from the model, observational and reanalysis data sets (Kunze et al.,
307 2016; Santee et al., 2017; Yuan et al., 2019). In this present study, we have investigated the
308 spatial variability, trends of the anticyclone and the influence of Indian monsoon activity i.e.
309 active and break days, strong and weak monsoon years, and strong La Niña and El Niño years
310 on ASMA using long-term reanalysis, satellite and observational data sets that were not
311 investigated earlier. In this study, we have considered the GPH values from 16.75 km to 16.9
312 km, which represents the spatial structure of the anticyclone at 100 hPa. Our analysis shows
313 that the spatial extent (magnitude) of the anticyclone structure is very large (strong) during
314 July followed by August whereas it is very weak in June at 100 hPa. The bimodal distribution
315 (Tibetan and Iranian modes) of the anticyclone is clearly observed during the month of July
316 which is absent during other months (June and August). The anticyclone variability
317 undergoes significant decadal variations from one decade to another. The edges of ASMA
318 changes drastically compared to the core of the anticyclone. However, there are significant
319 spatial differences in the structure of the anticyclone at 100 hPa. The anticyclone undergoes a
320 decreasing trend on the northern side whereas an increasing trend on the western part. A
321 significant increasing trend is observed in the spatially averaged zonal wind in four different
322 sectors (Figure 5). The zonal wind anomalies show increasing trend in all the sectors at 100
323 hPa. The change is significant in the north-western and north-eastern sectors with a
324 magnitude variability of 7.59 m/s from 1951-2016 whereas it is 5.44 m/s in the south-eastern
325 and south-western sectors. The strength of the anticyclone increases with a rate of 0.157 m/s
326 per year (10.36 m/s from 1951-2016) in the anticyclone region (Figure 5e). Yuan et al. (2019)

327 also reported the increasing trend in the strength of the anticyclone by considering the
328 MERRA 2 reanalysis data from 2001-2015.

329 Further, we have investigated the Indian monsoon influence on the anticyclone region.
330 Our results reveal that the spatial extent of the anticyclone expands during the active phase of
331 the Indian monsoon, the strong monsoon years and during strong La Niña years on the
332 northern and eastern sides. A similar expansion of the anticyclone is noticed during strong
333 monsoon years from MERRA2 data by Yuan et al. (2019). However, the ASMA boundaries
334 are not always well defined in all the events. The zonal mean cross-section of temperature
335 shows significant warming over the Tibetan Plateau and from the surface to 12 km during the
336 active phase of the Indian monsoon, the strong monsoon years, and the strong La Niña years.
337 Similarly, the rise of tropopause during the active phase of the Indian monsoon, the strong
338 monsoon years and the strong La Niña years are noticed. Since the Tibetan Plateau acts as a
339 strong heat source in summer with the strongest heating layer lying in the lower layers, the
340 thermal adaptation results in a shallow and weak cyclonic circulation near the surface, and a
341 deep and strong anti-cyclonic circulation above it. During summer, the Tibetan Plateau acts
342 as a strong heat source, which influences the whole UTLS region. The warm ascending air
343 above will pull the air from below; the surrounding air in the lower troposphere converges
344 towards the Tibetan Plateau area and climbs up the heating sloping surfaces (Bergman et al.,
345 2013; Garny and Randel, 2016). Significant warming is observed over the Tibetan Plateau,
346 which represents the strong transport of pollutants into the tropopause during the active phase
347 of the Indian monsoon, the strong monsoon years, and the strong La Niña years. Pan et al.
348 (2016) reported the transport of carbon monoxide through the southern flank of the Tibetan
349 Plateau from the model analysis. The above-mentioned results indicate that the high
350 mountain regions play a significant role in elevated heat sources during the formation and
351 maintenance of the anticyclones over Asia. It emphasizes the role of the thermal forcing of

352 the Tibetan Plateau on the temporal and the spatial evolution of the South Asian High. Lau et
353 al. (2018) showed that the transport of the dust and pollutants from the Himalayas-Gangetic
354 Plain and the Sichuan Basin.

355 Overall, we demonstrate the ASMA variability during different phases of the Indian
356 monsoon. The uplifting of boundary layer pollutants to the tropopause level occurs primarily
357 on the eastern side of the anticyclone, centered near the southern flank of the Tibetan Plateau,
358 north-eastern India, Nepal, and north of the Bay of Bengal. The variability of tropopause
359 altitude and temperature, trace gases (Water Vapour (WV), Ozone (O₃), Carbon Monoxide
360 (CO) and aerosols (Attenuated Scattering Ratio (ASR) shows distinct in picture in ASMA
361 region. The ASMA itself is highly dynamical in nature and the confinement of tracers and
362 aerosols results in changes in its chemistry and radiation (Basha et al., 2019) However, a
363 more detailed and higher quality of the dataset is needed to further understand the effects of
364 the Tibetan Plateau on the transport of different tracers and pollutants to the UTLS region
365 (Ravindrababu et al., 2019).

366
367 *Data Availability.* The NCEP/NCAR reanalysis data are available from NOAA website
368 (<https://www.esrl.noaa.gov/psd/data/gridded/data.ncep.reanalysis.pressure.html>). The
369 COSMIC and CHAMP data is available from COSMIC CDAAC website. IMD gridded
370 precipitation data is available at National Climate data center Pune, India. All the data used in
371 the present study is available freely from the respective websites.

372 *Authors' Contributions.* GB and MVR conceived and designed the scientific questions
373 investigated in the study. GB performed the analysis and wrote the draft in close association
374 with MVR. PK estimated the active and break spells of the Indian monsoon. All authors
375 edited the paper.

376 *Competing Interests.* The authors declare that they have no competing financial interests.

377 *Acknowledgements.* We thank NCEP/NCAR reanalysis for providing reanalysis data. We
378 thank CDAAC for production of COSMIC and CHAMP GPSRO data and IMD gridded
379 precipitation data from National Climate data center Pune, India. This work was supported by
380 National Atmospheric Research Laboratory, Department of Space, and India

381 **References**

- 382 Anthes, R. A., Bernhardt, P. A., Chen, Y., Cucurull, L., Dymond, K. F., Ector, D., Healy, S.
383 B., Ho, S.-H., Hunt, D. C., Kuo, Y.-H., Liu, H., Manning, K., McCormick, C., Meehan, T.
384 K., Randel, W. J., Rocken, C., Schreiner, W. S., Sokolovskiy, S. V., Syndergaard, S.,
385 Thompson, D. C., Trenberth, K. E., Wee, T.-K., Yen, N. L., and Zeng, Z.: The
386 COSMIC/Formosat/3 mission: Early results, *B. Am. Meteorol. Soc.*, 89, 313–333, 2008.
- 387 Rao, D. N., Ratnam, M. V., Mehta, S., Nath, D., Ghouse Basha, S., Jagannadha Rao, V. V.
388 M., Krishna Murthy, B. V., Tsuda, T., and Nakamura, K.: Validation of the COSMIC
389 radio occultation data over Gadanki (13.48 N, 79.2 E): A tropical region, *Terr. Atmos.*
390 *Ocean. Sci.*, 20, 59–70, doi:10.3319/TAO.2008.01.23.01(F3C), 2009.
- 391 Baldwin, M. P., Gray, L. J., Dunkerton, T. J., Hamilton, K., Haynes, P. H., Randel, W. J.,
392 Holton, J. R., Alexander, M. J., Hirota, I., Horinouchi, T., Jones, D. B. A., Kinniersley, J.
393 S., Marquardt, C., Sato, K., and Takahashi, M.: The quasi-biennial oscillation, *Rev.*
394 *Geophys.*, 39, 179–229, doi:10.1029/1999RG000073, 2001.
- 395 Basha, G., Kishore, P., Ratnam, M.V., Ouarda, T.B.M.J., Velicogna, I., and Tyler Sutterly.:
396 Vertical and latitudinal variation of the intertropical convergence zone derived using GPS
397 radio occultation measurements, *Remote Sensing of Environment*,
398 <http://dx.doi.org/10.1016/j.rse.2015.03.024>, 2015.
- 399 Basha, G. and Ratnam, M. V.: Moisture variability over Indian monsoon regions observed
400 using high resolution radiosonde measurements, *Atmos. Res.*, 132–133, 35–45,
401 <https://doi.org/10.1016/j.atmosres.2013.04.004>, 2013.

402 Basha, G., Kishore, P., Ratnam, M. V., Jayaraman, A., Kouchak, A. A., and Taha, B.J. M.:
403 Historical and projected surface temperature over India during the 20th and 21st century.
404 *Scientific Reports*, 7(1), 2987. <https://doi.org/10.1038/s41598-017-02130-3>, 2017.

405 Basha, G., Ratnam, M. V., Kishore, P., Ravindrababu, S., and Velicogna, I.: Influence of
406 Asian Summer Monsoon Anticyclone on the Trace gases and Aerosols over Indian region,
407 *Atmos. Chem. Phys. Discuss.*, <https://doi.org/10.5194/acp-2019-743>, in review, 2019.

408 Bergman, J. W., Fierli, F., Jensen, E. J., Honomichl, S., and Pan, L. L.: Boundary layer
409 sources for the Asian anticyclone: Regional contributions to a vertical conduit, *J. Geophys.*
410 *Res.*, 118, 2560–2575, <https://doi.org/10.1002/jgrd.50142>, 2013.

411 Beyerle, G., Schmidt, T., Wickert, J., Heise, S., Rotacher, M., Koenig-Langlo, G., and
412 Lauritsen, K. B.: Observations and simulations of receiver-induced refractivity biases in
413 GPS radio occultation, *J. Geophys. Res.*, 111, D12101, doi:10.1029/2005JD006673. 2006.

414 Bian, J., Pan, L. L., Paulik, L., Vömel, H., and Chen, H.: In situ water vapor and ozone
415 measurements in Lhasa and Kunmin during the Asian summer monsoon, *Geophys. Res.*
416 *Lett.*, 39, L19808, doi:10.1029/2012GL052996, 2012.

417 Bromwich, D. H., Fogt, R. L., Hodges, K. I., and Walsh, J. E.: A tropospheric assessment of
418 the ERA-40, NCEP, and JRA-25 global reanalyses in the polar regions, *J. Geophys. Res.-*
419 *Atmos.*, 112, D10111, doi:10.1029/2006JD007859, 2007.

420 Fadnavis, S., Schultz, M. G., Semeniuk, K., Mahajan, A. S., Pozzoli, L., Sonbawne, S.,
421 Ghude, S. D., Kiefer, M., and Eckert, E.: Trends in peroxyacetyl nitrate (PAN) in the
422 upper troposphere and lower stratosphere over southern Asia during the summer monsoon
423 season: regional impacts, *Atmos. Chem. Phys.*, 14, 12 725–12 743,
424 <https://doi.org/10.5194/acp-14-12725-2014>, 2014.

425 Garny, H. and Randel, W. J.: Dynamic variability of the Asian monsoon anticyclone
426 observed in potential vorticity and correlations with 5 tracer distributions, *J. Geophys.*
427 *Res.*, 118, 13 421–13 433, <https://doi.org/10.1002/2013JD020908>, 2013.

428 Garny, H. and Randel, W. J.: Transport pathways from the Asian monsoon anticyclone to the
429 stratosphere, *Atmos. Chem. Phys.*, 16, 2703-2718, [https://doi.org/10.5194/acp-16-2703-](https://doi.org/10.5194/acp-16-2703-2016)
430 2016, 2016.

431 Glatthor, N., Höpfner, M., Stiller, G. P., von Clarmann, T., Funke, B., Lossow, S., Eckert, E.,
432 Grabowski, U., Kellmann, S., Linden, A., Walker, K. A., and Wiegele, A.: Seasonal and
433 interannual variations in HCN amounts in the upper troposphere and lower stratosphere
434 observed by MIPAS, *Atmos. Chem. Phys.*, 15, 563–582, [https://doi.org/10.5194/acp-15-](https://doi.org/10.5194/acp-15-563-2015)
435 563-2015, 2015.

436 Gottschaldt, K.-D., Schlager, H., Baumann, R., Cai, D. S., Eyring, V., Graf, P., Grewe, V.,
437 Jöckel, P., Jurkat-Witschas, T., Voigt, C., Zahn, A., and Ziereis, H.: Dynamics and
438 composition of the Asian summer monsoon anticyclone, *Atmos. Chem. Phys.*, 18, 5655-
439 5675, <https://doi.org/10.5194/acp-18-5655-2018>, 2018.

440 Hossaini, R., Chipperfield, M., Montzka, M. P., Rap, S. A., Dhomse, S., and Feng, W.:
441 Efficiency of short-lived halogens at influencing climate through depletion of stratospheric
442 ozone, *Nature Geoscience*, 8, 186–190, <https://doi.org/10.1038/ngeo2363>, 2015.

443 Hoskins, B. J., and Rodwell, M. J.: A model of the Asian summer monsoon, I: The global
444 scale, *J. Atmos. Sci.*, 52, 1329–1340, 1995.

445 Highwood, E. J. and Hoskins, B. J.: The tropical tropopause, *Q. J. Roy. Meteor. Soc.*, 124,
446 1579–1604, 1998.

447 Houze, R. A., Wilton, D. C., and Smull, B. F.: Monsoon convection in the Himalayan region
448 as seen by the TRMM 345 Precipitation Radar, *Q. J. Roy. Meteor. Soc.*, 133, 1389-1411,
449 [10.1002/qj.106](https://doi.org/10.1002/qj.106), 2007.

450 Hu, Y. and Pan, L.: Arctic stratospheric winter warming forced by observed SSTs, *Geophys.*
451 *Res. Lett.*, 36, L11707, doi:10.1029/2009GL037832, 2009.

452 Kishore, P., Ratnam, M. V., Namboothiri, S., Velicogna, I., Basha, G., Jiang, J., Igarashi, K.,
453 Rao, S., and Sivakumar, V.: Global (50° S–50° N) distribution of water vapor observed by
454 COSMIC GPS RO: Comparison with GPS radiosonde, NCEP, ERAInterim, and JRA-25
455 reanalysis data sets, *J. Atmos. Sol.-Terr. Phys.*, 73, 1849–1860,
456 doi:10.1016/j.jastp.2011.04.017, 2011.

457 Kishore, P., Jyothi, S., Basha, G., Rao, S.V.B., Rajeevan, M., Velicogna, I., and Sutterley,
458 T.C.: Precipitation climatology over India: validation with observations and reanalysis
459 datasets and spatial trends. *ClimDyn* 121. doi: [10.1007/s00382-015-2597-y](https://doi.org/10.1007/s00382-015-2597-y), 2015.

460 Kishore, P., Basha, G., VenkatRatnam, M., Velicogna, I., Ouarda, T. B. M. J., and Narayana
461 Rao, D.: Evaluating CMIP5 models using GPS radio occultation COSMIC temperature in
462 UTLS region during 2006–2013: twenty-first century projection and trends, *Clim.*
463 *Dynam.*, 47, 3253–3270, <https://doi.org/10.1007/s00382-016-3024-8>, 2016.

464 Kalnay, E., Kanamitsu, M., Kistler, R., Collins, W., Deaven, D., Gandin, L., Iredell, M.,
465 Saha, D., White, G., Woollen, J., Zhu, Y., Chelliah, M., Ebisuzaki, W., Higgins, W.,
466 Janowiak, J., Mo, K.C., Ropelewski, C., Wang, J., Leetma, A., Reynolds, R., and Dennis,
467 J.: The NCEP/NCAR 40-years reanalysis project. *Bull. Am. Meteorol. Soc.* 77, 437–472.
468 1996.

469 Kursinski, E. R., Hajj, G. A., Schofield, J. T., Linfield, R. P., and Hardy, K. R.: Observing
470 Earth's atmosphere with radio occultation measurements using the Global Positioning
471 System, *J. Geophys. Res.-Atmos.*, 102, 23429–23465, 1997.

472 Kunze, M., Braesicke, P., Langematz, U., and Stiller, G.: Interannual variability of the boreal
473 summer tropical UTLS in observations and CCMVal-2 simulations, *Atmos. Chem. Phys.*,
474 16, 8695–8714, <https://doi.org/10.5194/acp-16-8695-2016>, 2016.

475 Lau, W.K.M., Cheng, Y., and Li, Z.: Origin, maintenance and variability of the Asian
476 Tropopause Aerosol Layer (ATAL): Roles of monsoon dynamics. *Sci. Rep.* 2018, 8, 3960.

477 McPhaden, M. J., Zebiak, S. E., and Glantz M. H. ENSO as an integrating concept in earth
478 science, *Science*, 314, 1740–1745, 2006.

479 Medina, S., Houze, R. A., Kumar, A., and Niyogi, D.: Summer monsoon convection in the
480 Himalayan region: terrain and land cover effects, *Q. J. Roy. Meteor.Soc.*, 136, 593-616,
481 10.1002/qj.601, 2010.

482 Narendra Reddy, N., Venkat Ratnam, M., Basha, G., and Ravikiran, V.: Cloud vertical
483 structure over a tropical station obtained using long-term high-resolution radiosonde
484 measurements, *Atmos. Chem. Phys.*, 18, 11709–11727, [https://doi.org/10.5194/acp-18-](https://doi.org/10.5194/acp-18-11709-2018)
485 11709-2018, 2018.

486 Pai, D.S., Sridhar, L., and Ramesh Kumar, M.R.: Active and break events of Indian summer
487 monsoon during 1901-2014. *ClimDyn* 46, 3921– 3939. [https://doi.org/10.1007/s00382-](https://doi.org/10.1007/s00382-015-2813-9)
488 015-2813-9, 2016.

489 Pan, L. L., Honomichl, S. B., Kinnison, D. E., Abalos, M., Randel, W. J., Bergman, J. W.,
490 and Bian, J.: Transport of chemical tracers from the boundary layer to stratosphere
491 associated with the dynamics of the Asian summer monsoon, *J. Geophys. Res. Atmos.*,
492 121, 14159-14174, 10.1002/2016JD025616, 2016.

493 Park, M., Randel, W. J., Gettleman, A., Massie, S. T., and Jiang, J. H.: Transport above the
494 Asian summer monsoon anticyclone inferred from Aura Microwave Limb Sounder tracers,
495 *J. Geophys. Res.*, 112, D16309, <https://doi.org/10.1029/2006JD008294>, 2007.

496 Rajeevan, M., Gadgil, S., and Bhate, J.: Active and break spells of the Indian summer
497 monsoon, *J. Earth Syst. Sci.*, 119, 229–247, doi:[10.1007/s12040-010-0019-4](https://doi.org/10.1007/s12040-010-0019-4), 2010.

498 Randel, W. J., and Park, M.: Deep convective influence on the Asian summer monsoon
499 anticyclone and associated tracer variability observed with Atmospheric Infrared Sounder
500 (AIRS), *J. Geophys. Res.*, 111, D12314, <https://doi.org/10.1029/2005JD006490>, 2006

501 Rao, D. N., Ratnam, M. V., Mehta, S., Nath, D., Ghouse Basha, S., Jagannadha Rao, V. V.
502 M., Krishna Murthy, B. V., Tsuda, T., and Nakamura, K.: Validation of the COSMIC
503 radio occultation data over Gadanki (13.48 N, 79.2 E): A tropical region, *Terr. Atmos.*
504 *Ocean. Sci.*, 20, 59–70, doi:10.3319/TAO.2008.01.23.01(F3C), 2009.

505 Ratnam, M. V., Sunilkumar, S., Parameswaran, K., Murthy, B. K., Ramkumar, G., Rajeev,
506 K., Basha, G., Babu, S. R., Muhsin, M., and Mishra, M. K.: Tropical tropopause dynamics
507 (TTD) campaigns over Indian region: An overview, *J. Atmos. Sol.-Terr. Phys.*, 121, 229–
508 239, 2014

509 RavindraBabu, S., VenkatRatnam, M., Basha, G., Krishnamurthy, B. V., and
510 Venkateswararao, B.: Effect of tropical cyclones on the tropical tropopause parameters
511 observed using COSMIC GPS RO data, *Atmos. Chem. Phys.*, 15, 10239–10249,
512 doi:10.5194/acp-15-10239-2015, 2015.

513 Ravindrababu, S., Ratnam, M.V., Basha, G., Liou, Y.-A., Reddy, N.N.: Large Anomalies in
514 the Tropical Upper Troposphere Lower Stratosphere (UTLS) Trace Gases Observed
515 during the Extreme 2015–16 El Niño Event by Using Satellite Measurements. *Remote*
516 *Sens.* 2019, 11(6), 687; <https://doi.org/10.3390/rs11060687>, 2019.

517 Riese, M., Ploeger, F., Rap, A., Vogel, B., Konopka, P., Dameris, M., and Forster, P.: Impact
518 of uncertainties in atmospheric mixing on simulated UTLS composition and related
519 radiative effects, *J. Geophys. Res.*, 117, D16305, <https://doi.org/10.1029/2012JD017751>,
520 2012.

521 Santee, M. L., Manney, G. L., Livesey, N. J., Schwartz, M. J., Neu, J. L., and Read, W. G.: A
522 comprehensive overview of the climatological composition of the Asian summer monsoon

523 anticyclone based on 10 years of Aura Microwave Limb Sounder measurements, J.
524 Geophys. Res.-Atmos., 122, 5491– 5514, <https://doi.org/10.1002/2016JD026408>, 2017

525 Schreiner, W., Rocken, C., Sokolovskiy, S., Syndergaard, S., and Hunt, D.: Estimates of the
526 precision of GPS radio occultations from the COSMIC/FORMOSAT-3 mission, Geophys.
527 Res. Lett., 34, L04808, doi:10.1029/2006GL027557, 2007.

528 Sokolovskiy, S. V., Kuo, Y.-H., Rocken, C., Schreiner, W. S., Hunt, D., and Anthes, R. A.:
529 Monitoring the atmospheric boundary layer by GPS radio occultation signals recorded in
530 the open-loop mode, Geophys. Res. Lett., 33, L12813, doi:10.1029/2006GL025955, 2006.

531 Solomon, S., Rosenlof, K., Portmann, R., Daniel, J., Davis, S., Sanford, T., and Plattner, G.-
532 K.: Contributions of stratospheric water vapor to 5 decadal changes in the rate of global
533 warming, Science, 327, 1219–1223, <https://doi.org/10.1126/science.1182488>, 2010

534 Tissier, A.-S., and Legras, B.: Convective sources of trajectories traversing the tropical
535 tropopause layer, Atmos. Chem. Phys., 16, 3383–3398, doi:10.5194/acp-16-3383-2016,
536 2016.

537 Trenberth, K. E.: Recent observed interdecadal climate changes in the Northern Hemisphere,
538 B. Am. Meteorol. Soc., 71, 988–993, doi:10.1175/1520-0477(1990)0712.0.CO;2, 1990.

539 Vernier, J. P., Fairlie, T. D., Natarajan, M., Wienhold, F. G., Bian, J., Martinsson, B. G.,
540 Crumeyrolle, S., Thomason, L.W., and Bedka, K. M.: Increase in upper tropospheric and
541 lower stratospheric aerosol levels and its potential connection with Asian pollution, J.
542 Geophys. Res., <https://doi.org/10.1002/2014JD022372>, 2015

543 Vogel, B., Günther, G., Müller, R., Groß, J.-U., Afchine, A., Bozem, H., Hoor, P., Krämer,
544 M., Müller, S., Riese, M., Rolf, C., Spelten, N., Stiller, G. P., Ungermann, J., and Zahn,
545 A.: Long-range transport pathways of tropospheric source gases originating in Asia into
546 the northern lower stratosphere during the Asian monsoon season 2012, Atmos. Chem.
547 Phys., 16, 15 301–15 325, <https://doi.org/10.5194/acp-16-15301-2016>, 2016.

548 Vogel, B., Günther, G., Müller, R., Grooß, J.-U., and Riese, M.: Impact of different Asian
549 source regions on the composition of the Asian monsoon anticyclone and of the
550 extratropical lowermost stratosphere, *Atmos. Chem. Phys.*, 15, 13 699–13 716,
551 <https://doi.org/10.5194/acp15-13699-2015>, [http://www.atmos-chem-](http://www.atmos-chem-phys.net/15/13699/2015/)
552 [phys.net/15/13699/2015/](http://www.atmos-chem-phys.net/15/13699/2015/), 2015.

553 Wickert, J., Reigber, C., Beyerle, G., König, R., Marquardt, C., Schmidt, T., Grunwaldt, L.,
554 Galas, R., Meehan, T. K., Melbourne, W. G., and Hocke, K.: Atmosphere sounding by
555 GPS radio occultation: First results from CHAMP, *Geophys. Res. Lett.*, 28, 3263–3266,
556 2001.

557 Xie, F., Li, J., Tian, W., Feng, J., and Huo, Y.: Signals of El Niño Modoki in the tropical
558 tropopause layer and stratosphere, *Atmos. Chem. Phys.*, 12, 5259–5273,
559 <https://doi.org/10.5194/acp-12-5259-2012>, 2012.

560 Yan, R.-C., Bian, J.-C., and Fan, Q.-J.: The impact of the South Asia high bimodality on the
561 chemical composition of the upper troposphere and lower stratosphere, *Atmos. Ocean. Sci.*
562 *Lett.*, 4, 229–234, 2011.

563 Yan, X., Konopka, P., Ploeger, F., Tao, M., Müller, R., Santee, M. L., Bian, J., and Riese, M.:
564 El Niño Southern Oscillation influence on the Asian summer monsoon anticyclone,
565 *Atmos. Chem. Phys.*, 18, 8079–8096, <https://doi.org/10.5194/acp-18-8079-2018>, 2018.

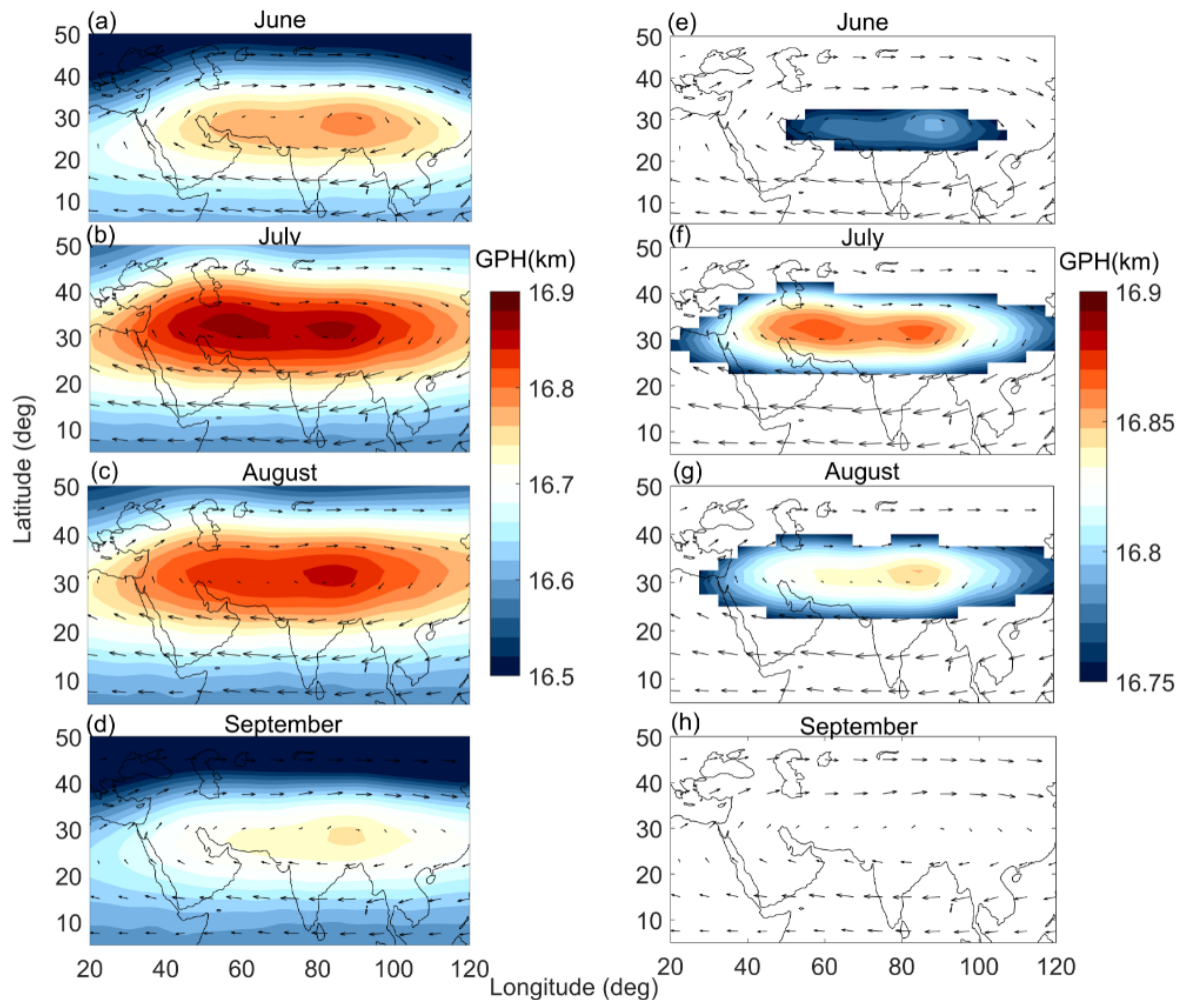
566 Yuan, C., Lau, W. K. M., Li, Z., and Cribb, M.: Relationship between Asian monsoon
567 strength and transport of surface aerosols to the Asian Tropopause Aerosol Layer (ATAL):
568 interannual variability and decadal changes, *Atmos. Chem. Phys.*, 19, 1901–1913,
569 <https://doi.org/10.5194/acp-19-1901-2019>, 2019.

570 Zhang, Q., Wu, G., and Qian, Y.: The Bimodality of the 100 hPa South Asia High and its
571 Relationship to the Climate Anomaly over East Asia in summer, *J. Meteorol. Soc. Jpn.*,
572 80, 733–744, 2002.

573 Zubiare, I., and Calvo, N.: The El Nino–Southern Oscillation (ENSO) Modoki signal in the
574 stratosphere, *J. Geophys. Res.*, 117, D04104, doi:10.1029/2011JD016690, 2012.

575

576



580 Figure 1. Spatial distribution of Geopotential Height (GPH) and wind vectors at 100 hPa

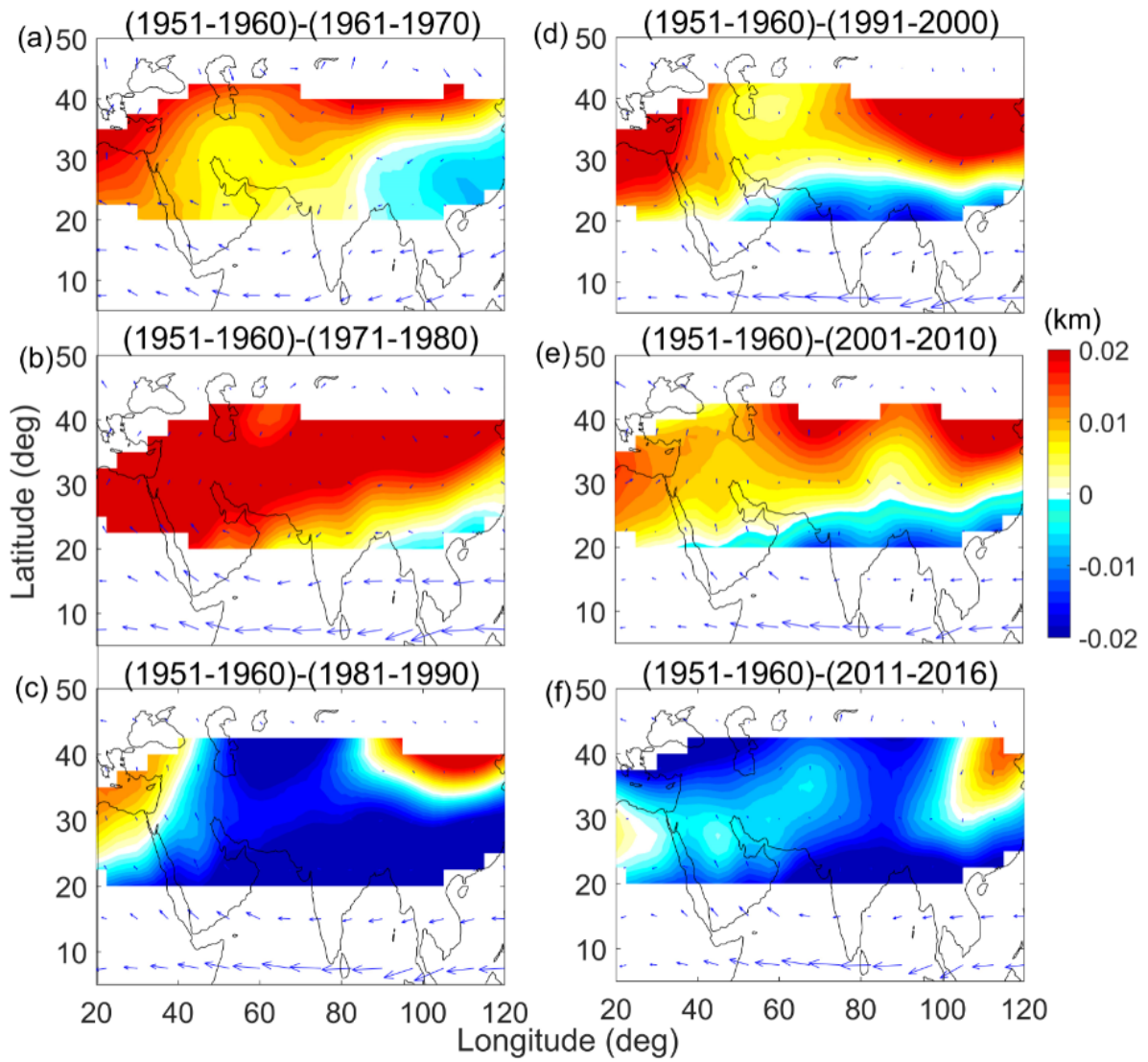
581 during (a) June, (b), July, (c) August and (d) September from NCEP reanalysis data

582 averaged from the year 1951-2016. The core of the anticyclone region was chosen based

583 on the GPH values ranging from 16.75 to 16.9 km. The spatial extent and magnitude of the

584 anticyclone after applying the GPH criteria for (e) June, (f) July, (g) August and (h),

585 September.



589

590 Figure 2. Decadal variation of anticyclone obtained from GPH and wind vectors with
 591 reference to 1951-1960 period.

592

593

594

595

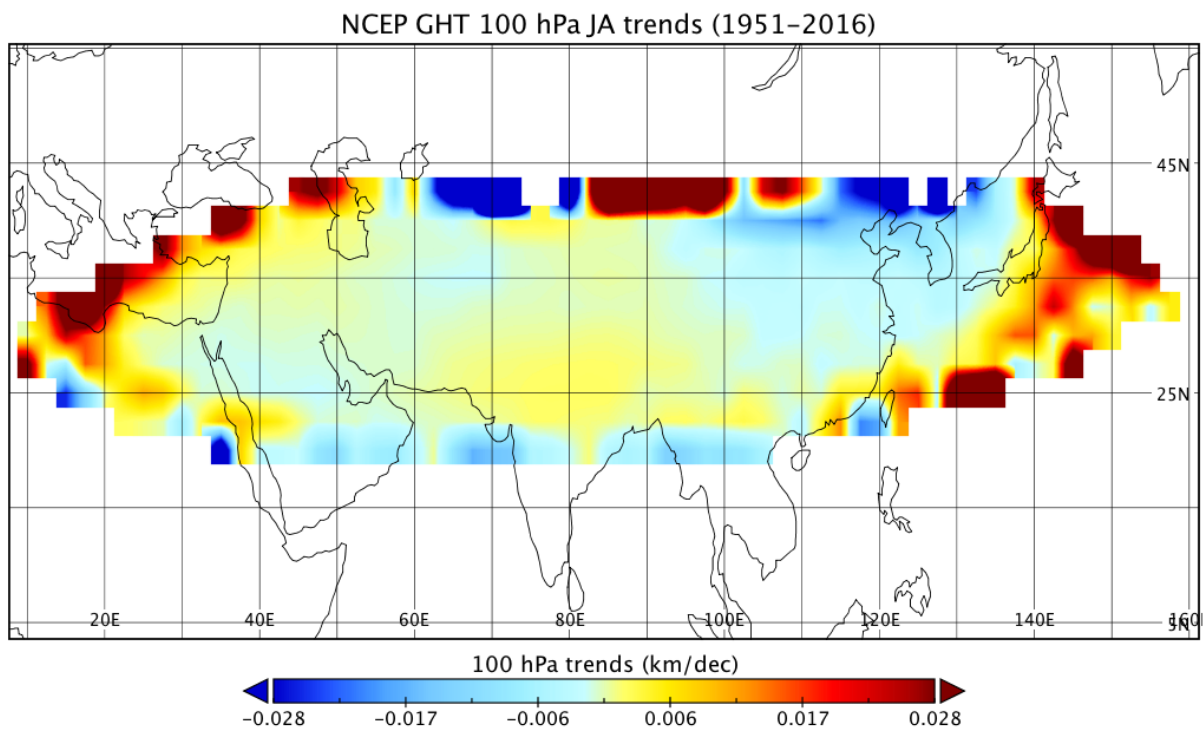
596

597

598

599

600



601

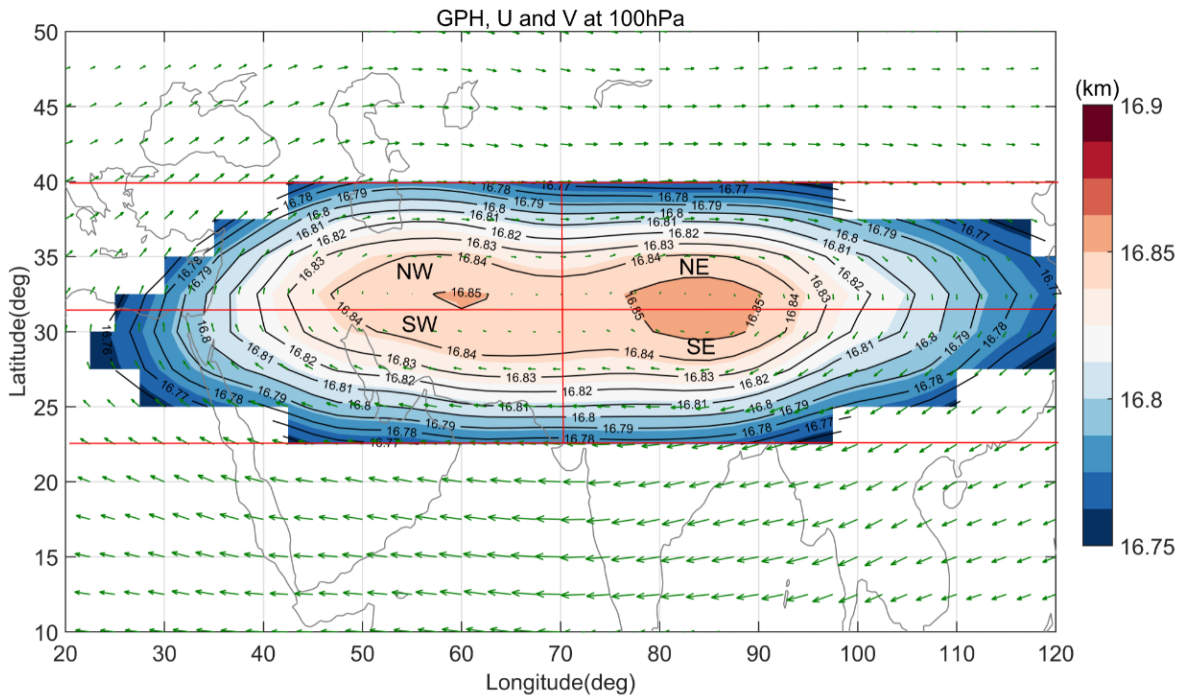
602

603 Figure 3. Spatial trend analysis obtained using robust regression analysis at 95% confidence
604 interval.

605

606

607



609

610 Figure 4. The climatological distribution of GPH (16.75 to 16.9 km) and wind vectors
 611 averaged during July and August from NCEP reanalysis data along with contour lines at
 612 100 hPa from 1951-2016. The anticyclone region is further divided into 4 sectors based
 613 on peak values of GPH. The GPH values peak centres at 32.5°N in latitude and 70°E in
 614 longitude. The sectors are further divided into South-East (SE) (22.5°N-32.5°N), North-
 615 East (NE) (32.5°N-40°N) in longitude band 70°E-120°E, South-West (SW) (22.5°N-
 616 32.5°N), and North-West (NW) (32.5°N-40°N) at 20°E-70°E longitude range.

617

618

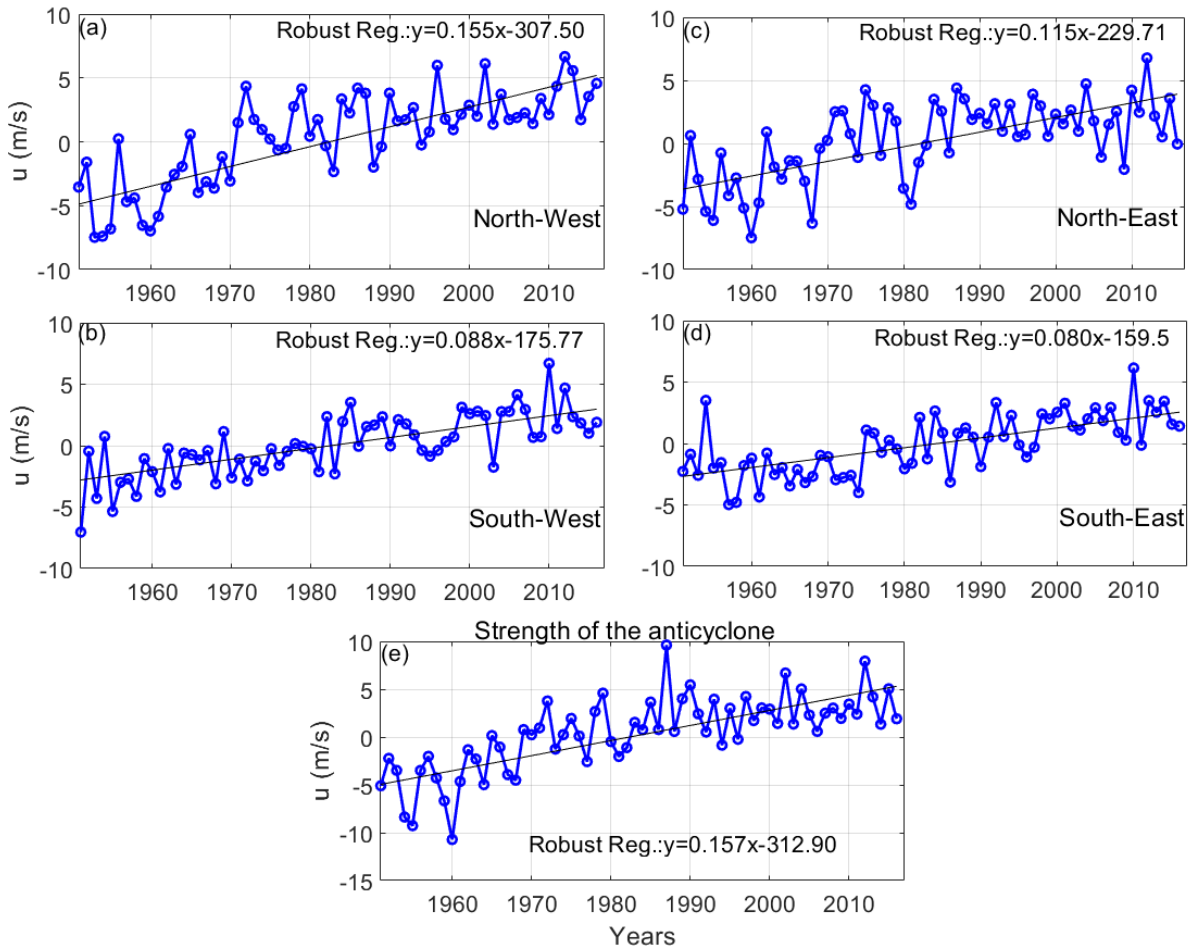
619

620

621

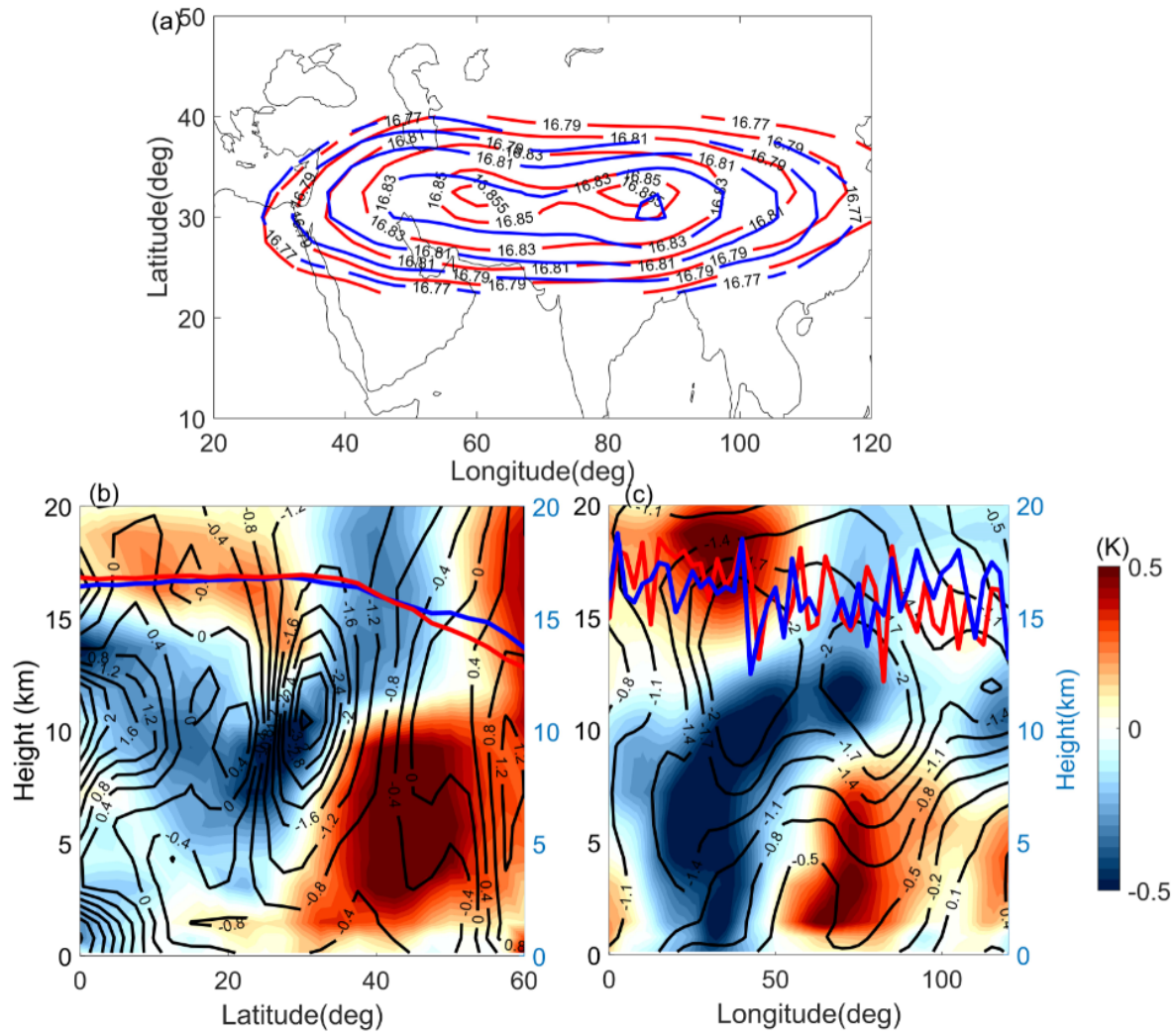
622

623



624

625 Figure 5. Time series of zonal wind anomalies estimated for (a) North-West, (b) South-West,
 626 (c) North-East and (d) South-East sectors of ASMA. The trend analysis was performed at
 627 95% confidence interval by using robust regression analysis. (e) The strength of the
 628 anticyclone was estimated from the zonal wind difference between (30°N-40°N)-(10°N-
 629 20°N) in the longitude band of 50°E-90°E.

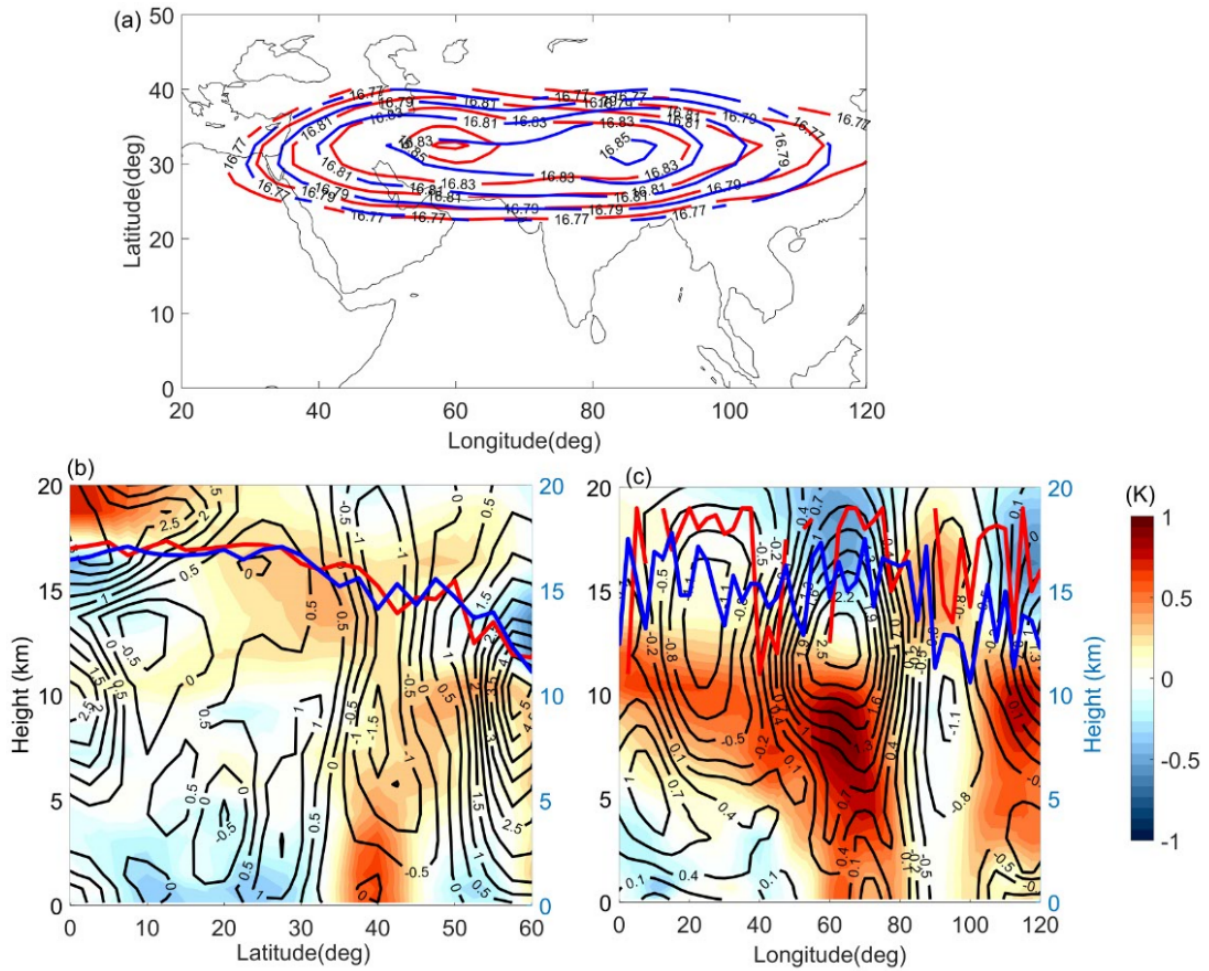


630

631 Figure 6. (a) ASMA variability during active and break phases of Indian monsoon obtained
 632 from GPH at 100 hPa. Red line indicates the active and blue line for break phase of Indian
 633 monsoon. (b) Latitude-altitude cross-section of temperature (colour shaded, K) and zonal
 634 wind anomalies (contour lines, m/s) which are estimated from difference between active
 635 and break phases of Indian Monsoon in the longitude band of 80°E-90°E. (c) Longitude-
 636 altitude cross-section of temperature and wind anomalies averaged between 30°N-40°N.
 637 The red and blue lines in Figure 6b & 6c denotes the tropopause altitude during active and
 638 break spells of Indian monsoon estimated using GNSS RO data, respectively.

639

640



641

642

643 Figure 7. (a) ASMA variability obtained from GPH at 100hPa during strong and weak

644 monsoon years calculated based on high resolution rainfall data in band of 5°N-30°N,

645 70°N-95°E grid. Red line indicates the strong and blue line for weak monsoon years. (b)

646 Latitude-altitude cross-section of temperature (colour shaded, K) and zonal wind

647 anomalies (contour lines, m/s) which are estimated from difference between strong and

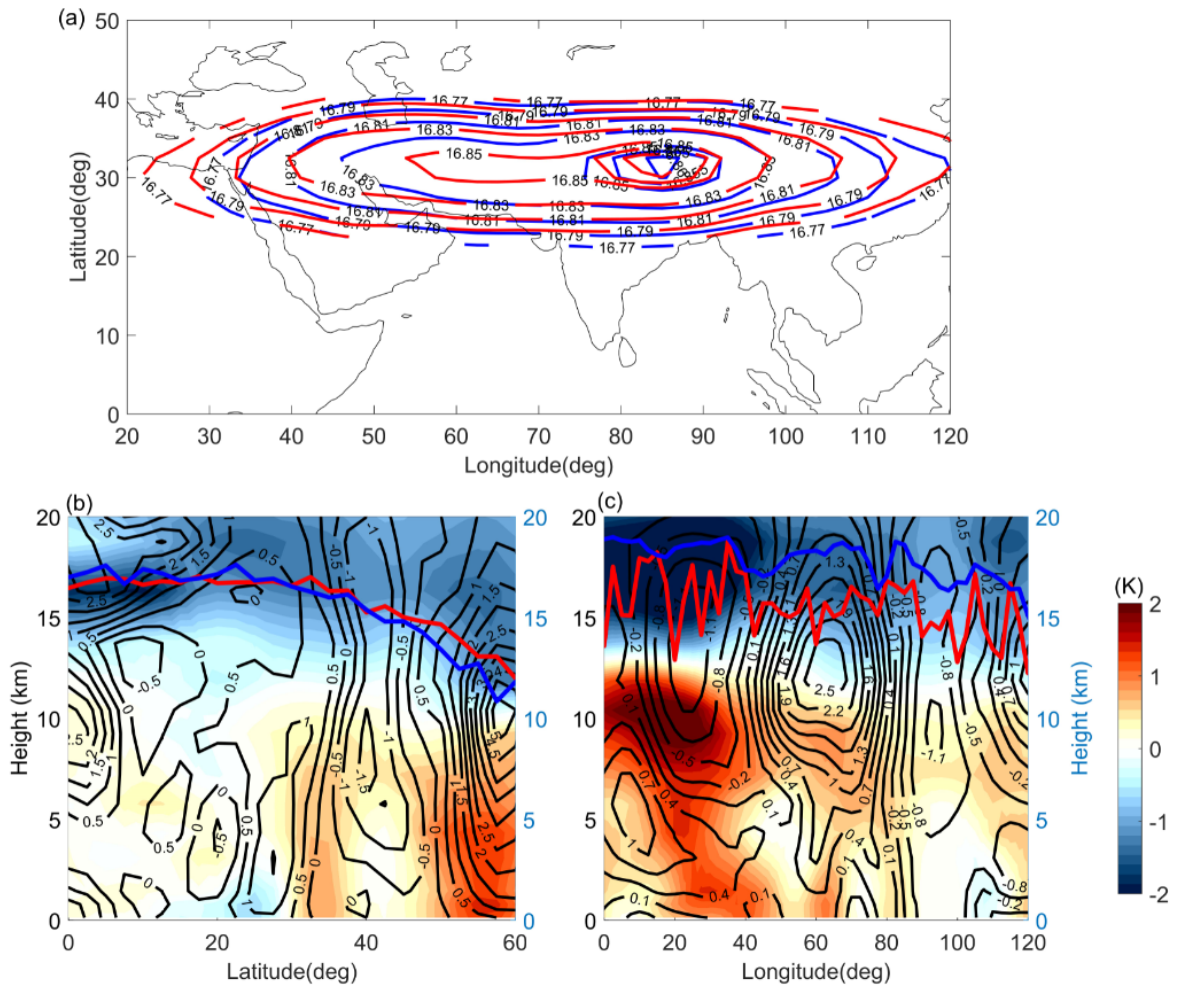
648 weak monsoon years in the longitude band of 80°E-90°E. (c) Longitude-altitude cross-

649 section of temperature and wind anomalies averaged between 30°N-40°N. Red and blue

650 lines in Figure 7b & 7c denote the tropopause altitude during strong and weak monsoon

651 years estimated using GNSS RO data, respectively.

652



654

655 Figure 8. (a) ASMA variability obtained from GPH at 100 hPa during strong La Niña and El
 656 Niño years. Red and blue lines indicate the La Niña and El Niño years. (b) Latitude-
 657 altitude cross-section of temperature (colour shaded, K) and zonal wind anomalies
 658 (contour lines, m/s) which are estimated from difference between La Niña and El Niño
 659 years in the longitude band of 80°E-90°E. (c) Longitude-altitude cross-section of
 660 temperature and zonal wind anomalies averaged between 30°N-40°N. The red and blue
 661 lines in Figure 8b & 8c denote the tropopause altitude during La Niña and El Niño years
 662 estimated from GNSS RO data, respectively.

663

664